Degradation of Carbon-Supported Platinum-Group-Metal Electrocatalysts in Alkaline Media Studied by in Situ Fourier Transform Infrared Spectroscopy and Identical-Location Transmission Electron Microscopy

Clémence Lafforgue, Frédéric Maillard, Vincent Martin, Laetitia Dubau, Marian Chatenet

Article

Degradation of Carbon-supported Platinum Group Metal Electrocatalysts in Alkaline Media Studied by in situ Fourier-Transform Infrared Spectroscopy and Identical-Location Transmission Electron Microscopy

Clémence Lafforgue, Frédéric Maillard, Vincent Martin, Laetitia Dubau, and Marian Chatenet

ACS Catal., **Just Accepted Manuscript** • DOI: 10.1021/acscatal.9b00439 • Publication Date (Web): 10 May 2019

Degradation of Carbon-supported Platinum Group Metal Electrocatalysts in Alkaline Media Studied by *in situ* Fourier-Transform Infrared Spectroscopy and Identical-Location Transmission Electron Microscopy

Clémence Lafforgue[1], Frédéric Maillard[1*], Vincent Martin[1], Laetitia Dubau[1], Marian Chatenet[1*]*

[1]Univ. Grenoble Alpes, Univ. Savoie Mont Blanc, CNRS, Grenoble INP, LEPMI, 38000 Grenoble, France

ABSTRACT

Alkaline fuel cells and electrolyzers attract increasing attention of the electrochemical community, and one of their supposed advantages is their larger electrode materials stability than for their proton-exchange membrane analogues. However, stability of the core materials of fuel cells and electrolyzers in alkaline environment is not granted and remains understudied so far. Herein, using *in situ* Fourier-transform infrared spectroscopy (FTIR), identical-location transmission electron microscopy (IL-TEM), X-ray photoelectron spectroscopy (XPS) and CO_{ads} stripping techniques, we provide physical and chemical evidences that Pt-based nanocatalysts catalyze the electrochemical corrosion of the carbon support (Vulcan XC72). This is due to more facile oxidation of oxygen-containing surface groups of the carbon support upon adsorption of

hydroxyl groups on the Pt-based surface. The degradation mechanism is, to some extent, similar for other carbon-supported Pt group metal (PGM) electrocatalysts. We propose that the extent of degradation of PGM/C nanoparticles in alkaline electrolytes scales with the electrocatalyst's activity to electrooxidize CO, thereby providing a marker of the materials propensity to degradation in alkaline environment.

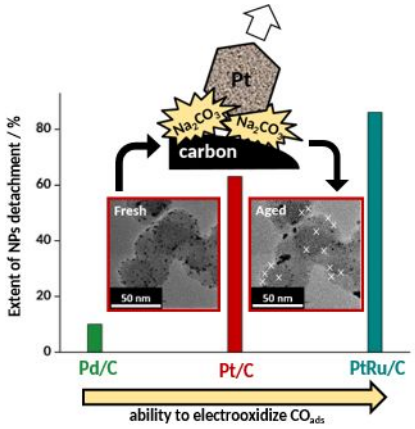

KEYWORDS

Alkaline Fuel Cells, Degradation Mechanism, PGM-containing Carbon-supported Electrocatalyst, Fourier-transform infrared spectroscopy, Identical-Location Transmission Electron Microscopy

1. INTRODUCTION

In an economic and environmental context where the usage of fossil energies must slow down, the scientific community is working hard on the development of alternative systems for energy storage and conversion. Electrolyzers and fuel cells are promising technologies of the sort, that

could enable long-term and large-scale storage of renewable electricity [1,2]. Among the wide range of fuel cells and electrolyzer systems, alkaline fuel cells (AFC) [3–6] and alkaline water electrolyzers (AWE) [7,8] have attracted increasing attention over the past few years due to their advantages with respect to acidic technologies: they benefit from faster oxygen reduction reaction (ORR) or oxygen evolution reaction (OER) kinetics, possibilities to use less platinum group metals (PGM) at their electrodes, a wide choice of fuel in addition to hydrogen (alcohol [9–11], sodium borohydride [12], hydrazine borane [13,14] can feed so-called direct liquid fuel AFC) and a wider range of polymer chemistries compared to proton exchange membranes [15,16].

However, very few studies have focused on the durability of the electrocatalysts used in AFC and AWE systems, the usual belief being that alkaline environment prevents severe degradations of electrode materials (for anion exchange membranes, the community is well aware of the issues at stake [17,18]). However, the durability of electrodes in alkaline environment is not granted, as already put forth in the past, both for PGM [19,20] and non-PGM [21] electrodes, at least in liquid hydroxide electrolytes. Based on these early studies, more systematic investigations were carried-out by us [22–25]. The results showed that Pt/C electrocatalysts undergo severe degradation upon potential cycling between high (1.2 V *vs.* the reversible hydrogen electrode, RHE) and low (0.1 V *vs.* RHE) potential limits, leading to a *ca.* 60 % loss of the electrochemical surface area (ECSA) that mostly results from detachment of the metal nanoparticles (NPs) from the carbon substrate. Interestingly, Raman and X-ray photoelectron spectroscopy (XPS) revealed that neither extensive carbon corrosion nor Pt dissolution could rationalize such degradations. According to the Pourbaix diagram [26], carbon is not stable in strong bases (pH = 14) above 0.06 V *vs.* RHE and forms dissolved carbonates (CO_3^{2-}) that spontaneously lead to surface passivation, by formation of solid alkali-metal carbonates (*e.g.* Na_2CO_3 or K_2CO_3 in NaOH or KOH electrolytes).

Nevertheless, this protection can be insufficient in strong bases, the pioneering work of Ross *et al*. [27–30] having shown that CO_2 formation (gasification, observed for $E > 1.5$ V and $T > 60$°C) or dissolution (observed for $E < 1.4$ V and $T < 50$°C) of carbon could proceed, both processes being likely promoted by the presence of 3d transition metals/oxides immobilized at the carbon. A deeper understanding was provided by a first run of *in situ* FTIR characterizations of the aging of Pt/C in 0.1 M NaOH during potential cycling between $0.1 < E < 1.2$ V *vs.* RHE: the formation of carbonates species was asserted [25]. In the same paper, the ECSA losses were also linked to the nature of the alkali metal cations (M) of the MOH electrolyte: Li^+, Na^+, K^+, and Cs^+ based electrolytes, for which the alkali metal carbonates are more soluble in the sequence Li^+, Na^+, K^+ to Cs^+, lead to decreasing ECSA losses. All these studies suggest that formation of solid carbonates in MOH electrolytes is favored at the Pt | carbon support interface, but fundamental insights about the degradation mechanism of PGM-electrocatalysts are still lacking.

Herein, FTIR experiments were conducted in a stepwise manner to detect precisely at which electrode potential carbonates do form. In addition, both the influence of Pt weight fraction (wt. %) and the nature of the metal NPs (Pd and PtRu in addition to Pt) were investigated, in the hope to (i) assert the degradation mechanism of Pt/C in base, but also to (ii) possibly generalize this proposed mechanism to the most studied carbon-supported PGM electrocatalysts in alkaline fuel cells and water electrolyzers.

2. EXPERIMENTAL SECTION

2.1 Electrocatalysts

The carbon-supported electrocatalysts were purchased from E-TEK or Premetek and used as received. They are all supported on Vulcan XC72 carbon black and are referred to as 10, 40 or 80 wt. % Pt/C, 10 or 40 wt. % PtRu/C and 10 or 40 wt. % Pd/C depending on the metal wt. %.

2.2 Morphological characterizations

TEM and IL-TEM observations were performed using a Jeol 2010 TEM apparatus equipped with a LaB_6 filament operating at 200 kV. In the case of the bimetallic PtRu/C electrocatalyst, scanning transmission electron microscopy (STEM) images and associated X-ray energy dispersive spectroscopy (X-EDS) elemental maps were acquired using a JEOL 2100F microscope operated at 200 kV equipped with a SDD Centurio retractable detector. The X-EDS spectra were recorded on selected zones of the TEM grid aged in Identical Location mode. The Pt *M* and Ru *L* lines were used to determine the elemental maps.

2.3 X-ray photoelectron spectroscopy (XPS)

XPS patterns were obtained using a Thermo Scientific K-alpha spectrometer with a monochromatized Al X-ray source (hν = 1486.6 eV; spot size = 400 µm). Pass energies of 30 and 100 eV were used to record the core level and the survey spectra, respectively. All spectra were acquired using an electron flood gun to compensate possible positive charge accumulation during measurements. The obtained spectra were deconvoluted and fitted using Thermo Scientific™ Advantage Software. The evolution of the oxygen content during the AST was monitored by dividing the peak areas of the O1s and the C1s signal (without the contribution of Nafion®-related envelopes), after proper background subtraction, by their respective atomic sensitivity factors:

$$ratio\left(\frac{O1s}{C1s}\right) = \frac{I_{O1s}}{0.63} * \frac{0.205}{I_{C1s}}$$

2.4 Electrochemical material

All the electrochemical measurements were performed using a Bio-Logic® potentiostat (SP300). The glassware and plastic accessories used for the experiments were soaked in Caro's acid (1-1 vol. % H_2O_2 (30 w/v %)-H_2SO_4 (> 95 wt. %)) overnight to prevent organic and metallic

pollution, and thoroughly rinsed with ultrapure water (18.2 MΩ cm, < 3 ppm Total Organic Carbon, Millipore Elix + Gradient, Millipore) prior being used.

The *in situ* FTIR spectroscopy measurements were conducted using a homemade three-electrode electrochemical cell. The counter electrode was a platinum mesh and the reference electrode was a freshly-prepared RHE. The electrolyte (0.1 M NaOH) was daily prepared using NaOH, H_2O crystals (Suprapur, Merck) dissolved in ultrapure water. The working electrodes were prepared using suspensions made of each of the electrocatalyst mentioned above, ultrapure water, 5 wt. % Nafion® solution and isopropyl alcohol (IPA) in quantities given in Table 1. After 20 min of sonication, the working electrodes were prepared by depositing 8 µL of the desired ink on a 1 cm-diameter gold electrode and then dried in an oven at T = 110°C. The same quantity of carbon was deposited on the gold electrode whatever the initial metal wt. %, so as to compare thin-film electrodes of the same thickness.

Table 1. Ink preparation for the FTIR experiments.

Commercial catalyst	Electrocatalyst (mg)	H_2O (µL)	Nafion® 5 wt. % (µL)	IPA (µL)
10 wt. % Pt/C E-TEK	10	5770	18.3	2000
40 wt. % Pt/C E-TEK	10	3590	41.2	1600
80 wt. % Pt/C E-TEK	10	1405	1.37	330
40 wt. % PtRu/C E-TEK	10	3590	41.2	1600
40 wt. % Pd/C Premetek	10	3590	41.2	1600

The CO_{ads} stripping experiments were conducted in a four-electrode electrochemical cell. The counter electrode was a glassy carbon plate, the reference electrode was a freshly prepared RHE and a gold wire was connected to the reference electrode via a capacitor bridge in order to avoid electrical noise [31]. The working electrodes were obtained by depositing 10 µL of a suspension (containing 10 mg of electrocatalyst, 1755 µL of ultrapure water, 61 µL of 5 wt. % Nafion® solution and 730 µL of IPA) on a 5 mm-diameter glassy-carbon electrode, yielding a loading of 20 $\mu g_{metal}\ cm_{geom}^{-2}$ to ease comparison between the various samples. This drop was then dried with a heat gun while the electrode was rotated, as recommended by Garsany *et al*. [32]. The electrolyte was 0.1 M NaOH and was daily prepared as described above. A similar electrochemical setup was used to perform the accelerated stress tests (AST), however, the working electrode was different: the electrocatalyst inks was deposited onto a gold TEM grid held in the electrolyte by two carbon plates to ensure electronic conduction.

2.5 Measurement protocols

FTIR measurements were performed using a Bruker Vertex 70V spectrometer. A CaF_2 prism beveled at 60° constituted the bottom of the electrochemical cell. The spectra were collected in external reflection using *p*-polarized light and a liquid-N_2-cooled MCT (Mercury-Cadmium-Telluride) detector. The single-beam spectra were obtained by co-adding 512 interferograms acquired at 4 cm^{-1} spectral resolution with an interferometer frequency of 40 kHz and then Fourier transformed.

For the *in situ* FTIR measurements, the working electrode was first introduced in the cell, and after 15 min of Ar bubbling, 5 cyclic voltammograms were recorded from E = 0.1 to 1.23 V *vs.* RHE at v = 50 mV s^{-1} in a hanging-meniscus configuration. Then, the working electrode was

pressed against the CaF_2 prism (thin layer configuration), its potential being maintained at E = 0.1 V *vs.* RHE. When an electrode position with an optimum reflectivity was obtained, 5 spectra were registered. Next, a succession of 100 mV steps increased the working electrode potential up to E = 1.2 V *vs.* RHE, an intermediate step to the low (control) potential E = 0.1 V *vs.* RHE being applied between each potential step. 512 interferograms were collected at each step and data were plotted using relative reflectivity R_E/R_{ref}, where R_E and R_{ref} are the reflectivity obtained at the desired potential (E = 0.2, 0.3, …, 1.2 V *vs.* RHE) and the reference potential (mainly 0.1 V *vs.* RHE), respectively. With this methodology, positive-going bands correspond to species consumption and negative-going bands correspond to species production.

For the *in situ* FTIR CO_{ads} stripping experiments, the electrolyte was purged with CO for 6 min, and then with Ar for 39 min to ensure that no dissolved CO remained in the bulk of the electrolyte. During this process, the working electrode was permanently pressed against the CaF_2 prism while keeping its potential at E = 0.1 V *vs*. RHE. Then, the same succession of potential steps as described above was applied.

The CO_{ads} stripping experiments conducted in the conventional cell were performed by bubbling CO for 6 min and then Ar for 39 min. Next, 3 cyclic voltammetry (CV) cycles were recorded between $0.1 < E < 1.33$ V *vs*. RHE at a potential sweep rate v = 20 mV s^{-1}.

The AST performed in this study consisted of 150 potential cycles between E = 0.1 and 1.23 V *vs.* RHE using a linear sweep ramp and v = 100 mV s^{-1}. The electrolyte was 0.1 M NaOH and the temperature T = 25°C.

3. RESULTS AND DISCUSSION

3.1 In situ FTIR spectroscopy on Pt/C

The FTIR spectra obtained under stepwise oxidation conditions on 10, 40 and 80 wt. % Pt/C in 0.1 M NaOH are shown in Figure 1. Four negative-going bands, located at 1380, 1610, 1710 and 1960 cm^{-1}, and one positive-going band at 1670 cm^{-1}, are noticed on 10 wt. % Pt/C. Similarly, the FTIR spectra measured on the 40 and 80 wt. % Pt/C are composed of five negative-going bands at 1310, 1390, 1580, 1730-1760 and 2010 cm^{-1} and one positive-going band at 1670 cm^{-1}.

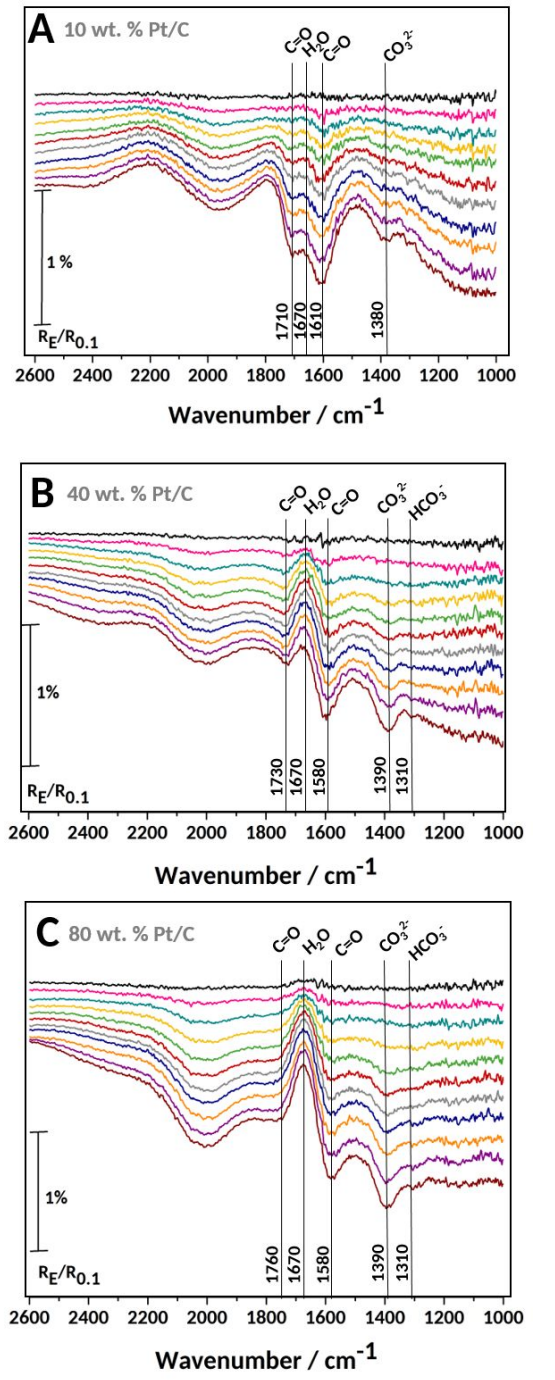
A
10 wt. % Pt/C
C=O
H2O
C=O
CO3 2-
1 %
RE/R0.1
1710
1670
1610
1380
2600 2400 2200 2000 1800 1600 1400 1200 1000
Wavenumber / cm-1
B
40 wt. % Pt/C
C=O
H2O
C=O
CO3 2-
HCO3-
1%
RE/R0.1
1730
1670
1580
1390
1310
2600 2400 2200 2000 1800 1600 1400 1200 1000
Wavenumber / cm-1
C
80 wt. % Pt/C
C=O
H2O
C=O
CO3 2-
HCO3-
1%
RE/R0.1
1760
1670
1580
1390
1310
2600 2400 2200 2000 1800 1600 1400 1200 1000
Wavenumber / cm-1
0.2 V vs. RHE
0.3 V vs. RHE
0.4 V vs. RHE
0.5 V vs. RHE
0.6 V vs. RHE
0.7 V vs. RHE
0.8 V vs. RHE
0.9 V vs. RHE
1.0 V vs. RHE
1.1 V vs. RHE
1.2 V vs. RHE

Figure 1. FTIR spectra obtained under stepwise oxidation conditions from E = 0.1 to 1.2 V *vs.* RHE in 0.1 M NaOH on A) 10 wt. % Pt/C, B) 40 wt. % Pt/C and C) 80 wt. % Pt/C (the relative reflectivity is calculated using the spectra obtained at E = 0.1 V *vs.* RHE as the reference reflectivity).

The band wavenumbers observed in these FTIR spectra and their corresponding assignment are sum up in Table 2.

Table 2. Band wavenumbers observed in FTIR spectra and their corresponding assignment.

Wavenumber / cm^{-1}	Bond	Mode	Assignment	Reference
1310	O=C-O	symmetric stretching	HCO_3^-	33–36
1380-1390	O=C-O	double degenerate stretching	CO_3^{2-}	33–40
1580 - 1610	C=O	stretching	quinone and/or carboxylate	41–46
1670	H-O-H	bending	H_2O	40
1710-1730-1760	C=O	stretching	carbonyl and carboxylic acid group	40,41,43–46
1960-2010			hydroxide/oxide adsorption on gold	

In agreement with past studies [33–40], the bands at 1380-1390 cm^{-1} and 1310 cm^{-1} were assigned to carbonate ions (CO_3^{2-}) and bicarbonate ions (HCO_3^-), respectively. For all the electrocatalysts, the intensity of the carbonate features increased along with an increase of the electrode potential: this strongly supports our former assumption [25] that the degradation of Pt/C NPs involves the production of carbonate ions. The impact of the Pt wt. % is also noticeable: the carbonate band (1380-1390 cm^{-1}) appears at E = 0.8 V *vs.* RHE for 10 wt. % Pt/C and at E = 0.5 V *vs.* RHE for 40 and 80 wt. % Pt/C. The area of this band was integrated at each electrode potential, as shown in Figure S1, and the results are displayed in Figure 2.They reveal that higher Pt ECSA enables

formation of carbonate species at lower potential (therefore quantitatively more carbonate formation at a given potential).

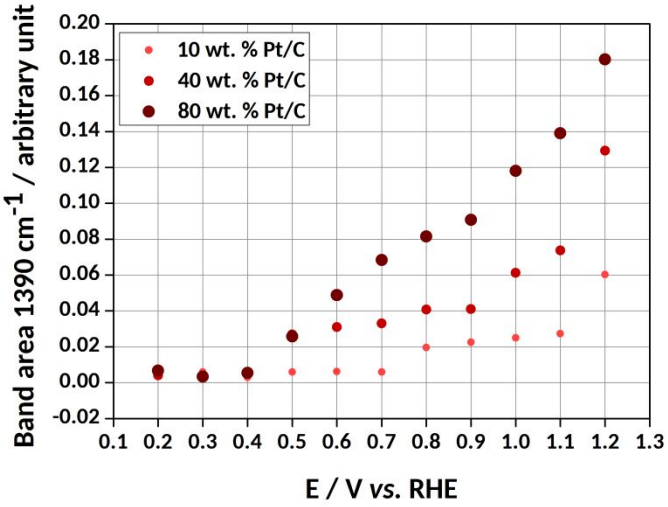

Figure 2. Area developed by the 1390 cm^{-1} band at different electrode potential on 10, 40 and 80 wt. % Pt/C.

The bands located at 1580-1610 cm^{-1} and 1710-1730-1760 cm^{-1} were assigned to oxygen-containing surface groups on carbon, namely quinone or carboxylate and carbonyl/carboxylic acid group, respectively [40–46]. As the standard potential of carbon oxidation reaction is $E^0 = 0.06$ V *vs.* RHE according to the Pourbaix diagram in alkaline media [26], the production of CO, CO_2, surface oxides or organic-carbon products are expected in the potential range investigated in this study ($0.1 < E < 1.2$ V *vs.* RHE). More practically, the band at 1710-1730-1760 cm^{-1} (carbonyl/carboxylic acid groups) appears at $E = 0.5$, 0.3 and 0.3 V *vs.* RHE for Pt/C 10, 40 and 80 wt. %, respectively, while the band at 1580-1610 cm^{-1} (quinone and/or carboxylate) appears at $E = 0.3$, 0.3 and 0.4 V *vs.* RHE for Pt/C 10, 40 and 80 wt. %, respectively. This means that, for all Pt/C electrocatalysts, oxygen-containing surface groups form on carbon at low potential ($0.2 < E < 0.6$ V *vs.* RHE, see Equation 1). Then, two *scenarios* can be considered. In *scenario* # 1,

these groups backspillover on the Pt NPs to create CO_{ads}-containing adsorbates (CO_{ads} and COH_{ads}, see Equation 2); when the potential exceeds 0.6 V *vs.* RHE, the CO_{ads}-containing adsorbates react with OH_{ads} species (via adsorption of OH^- ions, Equation 3) to form CO_2 (Equation 4), that converts into alkali-metal carbonates M_2CO_3 (M= Na in NaOH, K in KOH, etc.) (Equation 6). In *scenario* # 2, the oxygen-containing surface groups that form on the carbon near the Pt NPs are oxidized at high potential by combination with Pt-OH_{ads} (Equation 3 and 5) to form CO_2, that converts into solid carbonates (Equation 6). These two *scenarios* are both equally likely in the authors opinion and both allow rationalizing the destruction of the anchoring site between the NP and the carbon support.

$$C_n - C + 2OH^- \rightarrow C_n - CO_{ads} + H_2O + 2e^- \quad \text{Equation 1}$$

$$Pt + C_n - CO_{ads} \rightarrow Pt - CO_{ads} + C_n \quad \text{Equation 2}$$

$$Pt + OH^- \rightarrow Pt - OH_{ads} + e^- \quad \text{Equation 3}$$

$$Pt - CO_{ads} + Pt - OH_{ads} + OH^- \rightarrow CO_2 + H_2O + 2\,Pt \quad \text{Equation 4}$$

$$C_n - CO_{ads} + Pt - OH_{ads} + OH^- \rightarrow CO_2 + H_2O + Pt + C_n \quad \text{Equation 5}$$

$$CO_2 + 2\,OH^- \rightarrow CO_3^{2-} + H_2O \quad \text{Equation 6}$$

In the two suggested degradation mechanisms, water and carbonate species are supposed to be produced simultaneously. Thus, a negative-going band is expected for water bending at 1645 cm^{-1} [40]. This band is located at 1670 cm^{-1} in our study and points positive for the three electrocatalysts, which suggest consumption (or loss) of water. One possible explanation for the apparent consumption of water would imply a change of carbon surface properties from hydrophilic to hydrophobic. Indeed, it is well-known that oxygen-containing surface groups are present on the native carbon surface (Equation 1): the surface of the carbon support is thus necessarily hydrophilic in the fresh state. It is therefore expected that the consumption of these

oxygenated functions (Equation 2 and 5) leads to a change in its wetting properties. Because the thin layer formed between the electrode surface and the prism has a fixed volume and is diffusionally-isolated, the repulsion of water from the carbon support (C_n) occurring upon electrode potential increase would result in a positive-going water bending band at 1645 cm^{-1} in FTIR spectra. The higher this intensity, the more hydrophobic the carbon surface, as a result of the more pronounced corrosion of the oxygen-containing surface groups into CO_2 and production of metal carbonates. The corrosion of oxygen-containing surface groups also takes place in acidic media, as described recently in Refs [47,48].

According to the proposed mechanisms, two other species should have been detected: CO_2 and CO (only for *scenario* # 1). The main infrared spectroscopy features of these species are bands with strong intensities located at 2345 cm^{-1} and *ca*. 2045 cm^{-1} respectively [33,37,49,50], but none of them was detected in our study. This apparent discrepancy can be explained, though. Firstly, CO_2 is an intermediate species in the proposed corrosion mechanism but this product is rapidly converted to CO_3^{2-} in alkaline media. FTIR spectroscopy being a quasi-stationary measurement, the detection of transient species is very tricky, explaining the absence of CO_2 related bands in our experiments. Secondly, regarding the formation of CO in *scenario* # 1, it is postulated that too little CO is produced (well below a complete monolayer on the Pt NPs), because CO-containing groups mostly originate from a limited reservoir (the Pt | C interface) and are oxidized at potential above 0.4 V *vs*. RHE (Figure 1 and Figure 9). Hence in the conditions of our study, CO_{ads} species will hardly accumulate on the Pt surface.

Finally, according to FTIR measurements performed on polycrystalline gold (the electrode used for FTIR measurements) in the same conditions (Figure S2), the very broad negative-going band located around 2000 cm^{-1} on all the spectra might be assigned to a change of gold reflectivity

during the experiment (*e.g.* because gold progressively gets covered by OH_{ads} and/or surface oxides [51]). This broad band is noticeable on all the spectra presented in this study and the assignment is identical for all of them.

3.2 Additional investigations about the degradation mechanism

3.2.1 *In situ* FTIR spectroscopy and XPS measurement on Vulcan XC72

To confirm that the degradation of Pt/C electrocatalysts in alkaline media comes from a Pt-assisted local corrosion of the carbon support, similar FTIR experiments were performed on bare Vulcan XC72, and the results are presented in Figure 3. In addition, FTIR measurements on Vulcan XC72 using a more extensive AST (150 potential cycles between E = 0.1 and 1.23 V *vs.* RHE at v = 100 mV s^{-1}) were performed (Figure S3) and XPS measurement on bare Vulcan XC72 and 40 wt. % Pt/C were carried-out before and after the same AST procedure (Figure S4).

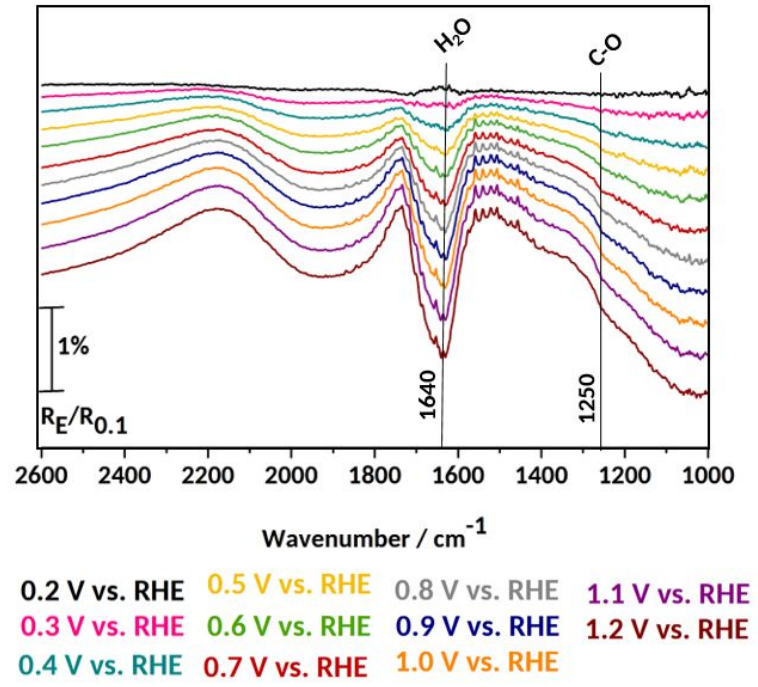

Figure 3. FTIR spectra obtained under stepwise oxidation conditions from E = 0.1 to 1.2 V *vs.* RHE in 0.1 M NaOH on Vulcan XC72 (the relative reflectivity is calculated using the spectra obtained at E = 0.1 V *vs.* RHE as the reference reflectivity).

During the stepwise oxidation, a very weak shoulder located at 1250 cm^{-1} develops on the FTIR spectra, which is assigned to C-O stretching [41]; a broad negative-going band located at 1640 cm^{-1} was assigned to H-O-H bending, signing water production. However, no band relative to carbonate species was detected, putting into evidence that no or limited quantities of (bi)carbonates are produced in the absence of Pt: this results supports our previous hypothesis that (bi)carbonates are formed following CO_2 production on Pt sites. Nevertheless, no band (other than the one located at 1250 cm^{-1}) related to oxygen-containing surface groups was detected in the absence of Pt NPs. It is possible that the bands linked to the oxygen-containing surface groups could be drowned in the broadband located at 1640 cm^{-1}, that may be dominated by the change of reflectivity of the Au substrate (see Figure S2).

These oxygen-containing surface groups are nevertheless observed on the FTIR spectra of the Vulcan XC72 carbon when it is submitted to a more extensive AST (150 potential cycles between E = 0.1 and 1.23 V *vs* RHE at v = 100 mV s^{-1}): bands located at 1590 cm^{-1} and 1740 cm^{-1} are clear on Figure S3, and they grow with the number of CV cycles performed. XPS measurements have also been performed pre and post 150 CV cycles of this AST for bare Vulcan XC72 and 40 wt.% Pt/C (Figure S4). The evolution of the oxygen content during AST was estimated using the O1s/C1s ratio (without the contribution of Nafion®-related envelopes and corrected from the atomic sensitivity factors). The O1s/C1s ratio increases from 0.10 to 0.18 upon the AST for Vulcan XC72, but remains stable for 40 wt. % Pt/C (O1s/C1s = 0.19 and 0.18 pre and post AST, respectively). This suggests that oxygen-containing surface groups do form and accumulate (their signature increases) on the carbon surface when Vulcan XC72 carbon is free of Pt NPs, whereas their proportion remains stable when Pt NPs are present, because the Pt NPs transform them into CO_2 and then carbonates upon their formation.

Another possible mechanism could be similar to that described by Yi and coworkers [52], who recently studied the electrochemical corrosion of glassy carbon (GC) in alkaline media. FTIR spectroscopy measurement on GC oxidized in alkaline media (U = 1.8 V *vs.* RHE during 24 hours in 0.1 M KOH) revealed no change compared to the pristine GC. Similarly, the Raman and XPS spectra and the cyclic voltammograms measured on the pristine and aged GC were nearly identical. To rationalize their findings, the authors postulated that the oxidation of GC in alkaline media occurs via a reaction of OH° radicals (produced by discharge of OH^- ions) with alkyl site chains, leading to transient oxidation of the edges of carbon layers until they become hydrophilic and dissolve, thus exposing a "fresh" GC surface.

3.2.2 CO_{ads}-electrooxidation on polycrystalline Pt

To support our hypotheses, the electrooxidation of a CO_{ads} monolayer in alkaline media was investigated on polycrystalline Pt. The results are displayed in Figure 4, and data are plotted using either the spectrum measured at E = 0.1 V *vs.* RHE (Figure 4-A) or that measured at E = 1.1 V *vs.* RHE (Figure 4-B) as a reference spectrum.

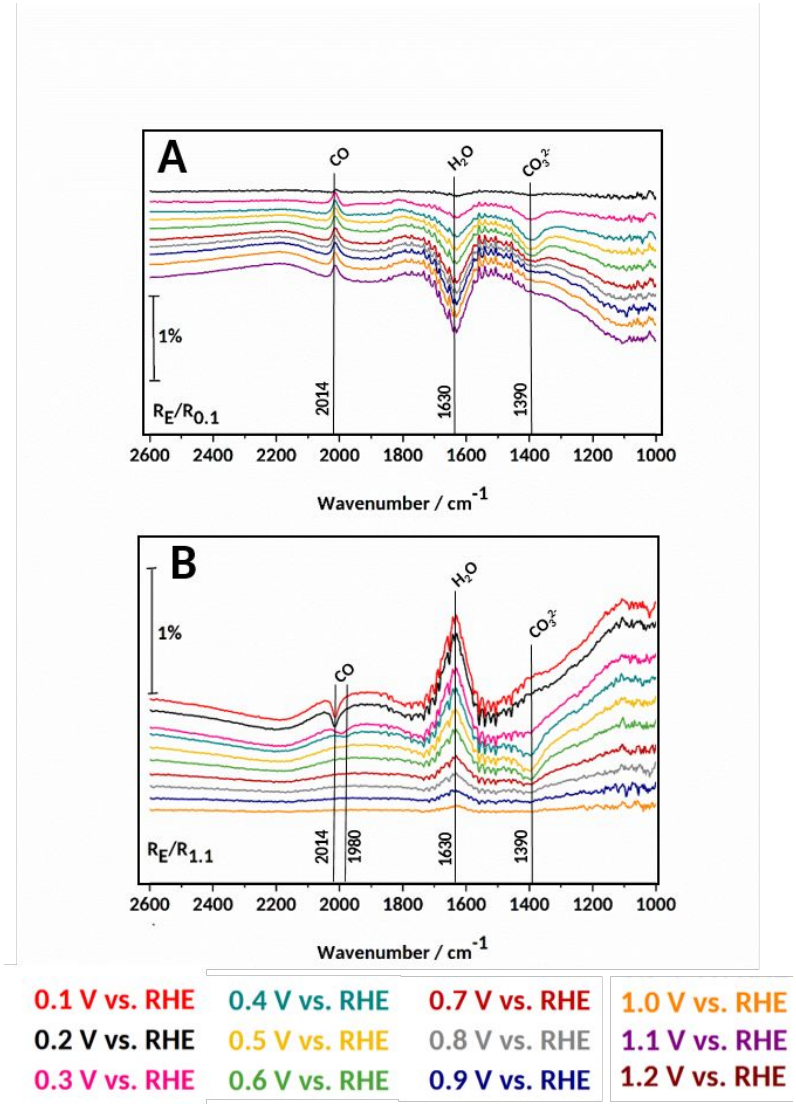

Figure 4. FTIR spectra obtained for CO_{ads} electrooxidation on polycrystalline Pt under stepwise oxidation conditions in 0.1 M NaOH. The electrode potential was stepped from E = 0.1 to 1.2 V *vs.* RHE; the relative reflectivity was calculated using the FTIR spectra obtained at A) E = 0.1 V *vs.* RHE and B) E = 1.1 V *vs.* RHE as the reference reflectivity.

Figure 4-A shows two negative-going bands located at 1390 and 1630 cm^{-1}, corresponding to carbonates and water production, respectively. Figure 4-B shows that CO_{ads} consumption is concomitant with CO_3^{2-} production: the CO_{ads} feature, located at 2014 cm^{-1} for E = 0.1 V *vs.* RHE

starts to disappear for 0.3 V *vs.* RHE and above, in parallel to the appearance of a positive band of water, sign of its generation in the process (as expected).

It is interesting to remark that carbonates are produced at lower potential on polycrystalline Pt relative to Pt/C electrocatalysts: the band at 1390 cm^{-1} is detected at E = 0.3 V *vs.* RHE on polycrystalline Pt, and at E = 0.8 or 0.5 V *vs.* RHE for Pt/C at low or high wt. %, respectively. Moreover, the carbonates feature grows up to E = 0.5 V *vs.* RHE and starts to decrease above E = 0.6 V *vs.* RHE on polycrystalline Pt (because the CO source is limited), whereas the band keeps growing on the Pt/C electrocatalysts (because the CO source is huge). Since all conditions were kept identical, this result nicely confirms that an equilibrium between the rate of carbonate formation and dissolution takes place in the thin layer formed between the electrode surface and the CaF_2 prism. In the CO_{ads} stripping experiment on polycrystalline Pt, the limited quantity of CO species facilitates the dissolution of carbonate species on the long term. In contrast, the corrosion of the carbon support promotes the renewal of a native carbon surface on Vulcan XC72, which is then oxidized into CO_2 and ultimately carbonate species. The process is operating until the Pt nanoparticle detaches from the support.

3.3 Towards a generalization of the mechanism: the case of PtRu/C and Pd/C

To generalize our findings, FTIR spectra were recorded on 40 wt. % PtRu/C and 40 wt. % Pd/C in the same experimental conditions (Figure 5). The high metal wt. % allowed highlighting whether these PGM catalyze the electrochemical corrosion of the carbon support. This is definitely the case for 40 wt. % PtRu/C. Indeed, four negative-going bands are observed on this catalyst (Figure 5-A), in particular the bands assigned to the presence of carbonate and bicarbonate ions. Similarly, Pd nanoparticles corrode the carbon support although to a minor extent: the band assigned to carbonates is indeed noticeable (Figure 5-B) but the intensity is very

weak. In addition, both FTIR spectra show the positive-going band assigned to water and located at 1670 cm^{-1}: the intensity of this band increases with the production of carbonates as observed previously with the three Pt/C electrocatalysts.

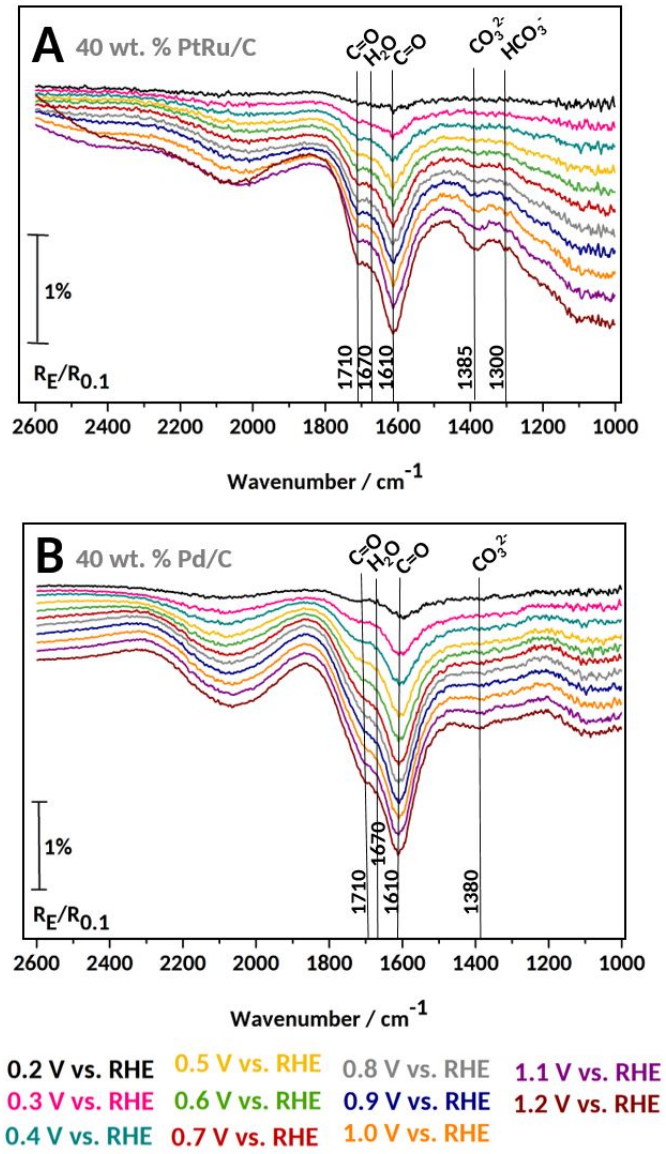

Figure 5. FTIR spectra obtained under stepwise oxidation conditions from E = 0.1 to 1.2 V *vs.* RHE in 0.1 M NaOH on A) 40 wt. % PtRu/C and B) 40 wt. % Pd/C; (the relative reflectivity is calculated using the spectra obtained at E = 0.1 V *vs.* RHE as the reference reflectivity).

The results were quantitatively confirmed by subjecting the three different materials to an accelerated stress test composed of 150 CV cycles between E = 0.1 and 1.2 V *vs.* RHE with a sweep rate of 100 mV s^{-1} in 0.1 M NaOH at T = 25°C. Meanwhile, IL-TEM images were

recorded on the fresh and aged catalysts in the exact same location (Figure 6). Note however that, to facilitate the visualization of the degradation and rebuild the particle size distributions, 10 wt. % catalysts were used. Figure 6-B-C reveals that the majority of the PtRu NPs are detached from the carbon support after the AST (highlighted with the white crosses – these do not pretend to be comprehensive) and that the remaining ones are agglomerated. More precisely, the extent of the NPs detachment reached 86 %. Furthermore, a metal deposit could be observed on the membrane of the TEM grid upon ageing (Figure 7 and Figure 8): X-EDS analyses revealed that this deposit is essentially composed of Ru. This finding is in line with the thermodynamic instability of Ru in alkaline environment [26] and illustrates the fact that Ru likely does not play any role in terms of COR catalysis. The more robust catalyst was clearly Pd/C for which only 10 % of the metal NPs were lost after the AST whereas 63 % are lost in the case of Pt/C. The evolution of the particle size distribution is overall similar for the three catalysts: the proportion of isolated big NPs lowers, while the proportion of isolated small NPs increases, suggesting that small particles are more stable than the big ones in these conditions. In the case of PtRu/C, this result could also result from the preferential dissolution of Ru during the AST.

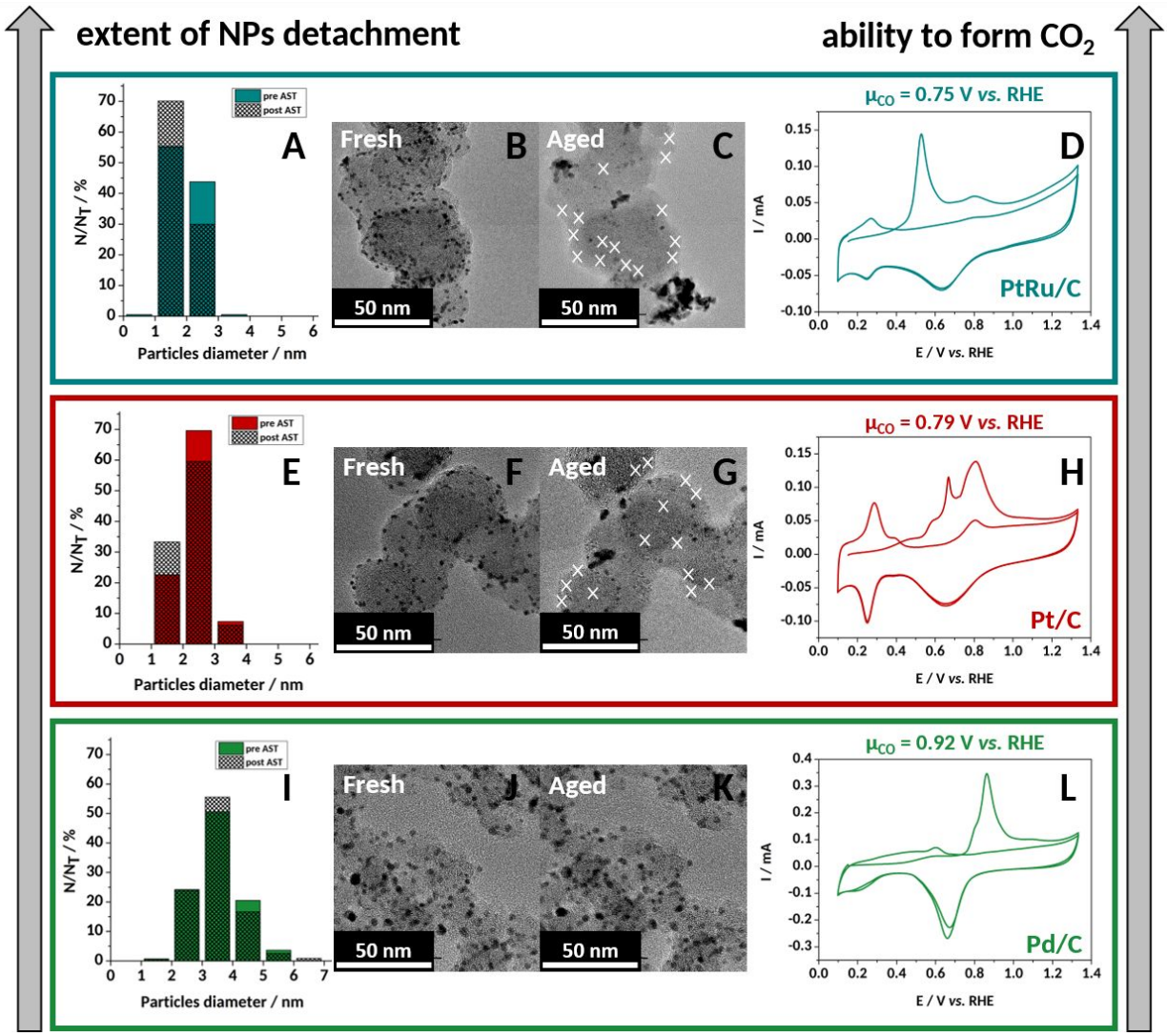

Figure 6. (A, E, I) Particle size distribution for 10 wt. % PtRu/C (blue), 10 wt. % Pt/C (red) and 10 wt. % Pd/C (green) electrocatalysts, N_T is the total number of counted particles (*ca.* 200). IL-TEM micrographs (B, F, J) pre-AST and (C, G, K) post-AST on 10 wt. % PtRu/C (blue), 10 wt. % Pt/C (red) and 10 wt. % Pd/C (green). (D, H, L) CO_{ads} stripping voltammograms recorded at v = 20 mV s^{-1} in 0.1 M NaOH on 10 wt. % PtRu/C (blue), 10 wt. % Pt/C (red) and 10 wt. % Pd/C (green).

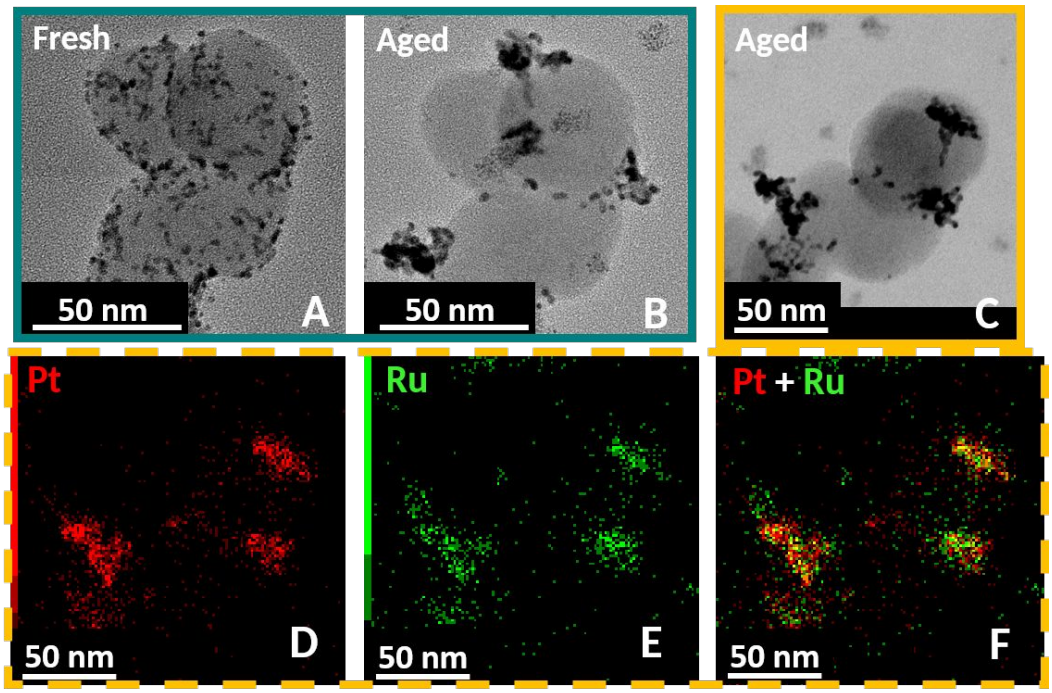

Figure 7. IL-TEM micrographs of the 10 wt. % PtRu/C A) pre and B) post AST. C) STEM images and (D, E, F) corresponding X-EDS maps obtained on aged PtRu/C after the AST.

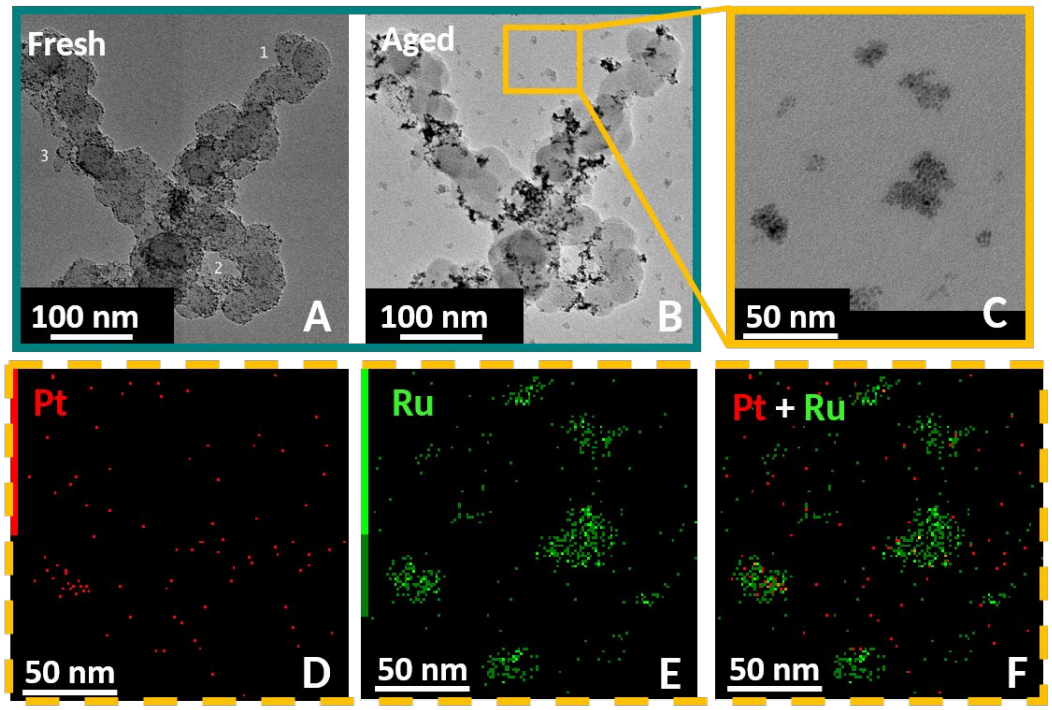

Figure 8. IL-TEM micrographs of the 10 wt. % PtRu/C A) pre and B) post AST. C) STEM images and (D, E, F) corresponding X-EDS maps of the deposit on the TEM grid after the AST.

Comparing IL-TEM images and CO_{ads} stripping voltammograms reveals particularly insightful: indeed the more corroded catalysts are those for which the metal has the larger propensity to electrooxidize CO (Figure 6-D-H-L) in 0.1 M NaOH. To quantitatively illustrate our hypotheses, the average CO_{ads} oxidation potential (μ_{CO}), first introduced by Chattot *et al.* [53], was extracted using the first moment of the potential weight:

$$\mu_{CO}\ (\mathrm{V}\ vs.\ \mathrm{RHE}) = \int \frac{E * I}{Q_{T,\ CO}} dE$$

where $Q_{T,\,CO}$ is the total electric charge of the CO_{ads} stripping voltammogram. The μ_{CO} values are 0.75, 0.79 and 0.92 V *vs.* RHE for PtRu/C, Pt/C and Pd/C, respectively. This indicates that the more active CO_{ads} oxidation electrocatalysts in alkaline media are respectively: PtRu/C > Pt/C >> Pd/C. Strikingly, the same ranking is obtained in terms of "extent of particles detachment".

Combining this result with the degradation monitored for the three electrocatalysts, we thus argue that the ability of an electrocatalyst to form CO_2 from CO_{ads} determines its degradation by detachment of the metal NPs upon potential cycling in alkaline electrolyte.

Finally, the areas of the band corresponding to carbonate groups were integrated for PtRu/C and Pd/C (Figure 9-A). The result show that, similarly to what was observed for 10 wt. % Pt/C, carbonate species are produced at potential above E = 0.8 V *vs.* RHE on PtRu/C. This is no surprise in view of the results of X-EDS elemental maps that showed that Ru atoms were dissolved during the AST, and hence did not contribute to the carbon support corrosion. In other words, the 40 wt. % PtRu/C catalyst finally behaves as a 20 wt. % Pt/C in terms of carbon support corrosion, which is confirmed by its intermediate situation in terms of carbonate production (Figure 9-A). On Pd/C, carbonate species are detected at E = 1.1 V *vs.* RHE.

The electrical charge corresponding to each potential step was also calculated. The results, shown in Figure 9-B, reveal that the charge obtained on PtRu/C is indeed higher to the one obtained on Pt/C and Pd/C because of the concomitance of Ru dissolution and carbonates production. We thus conclude that the degradation mechanism suggested for Pt/C is also essentially valid for PtRu/C and Pd/C.

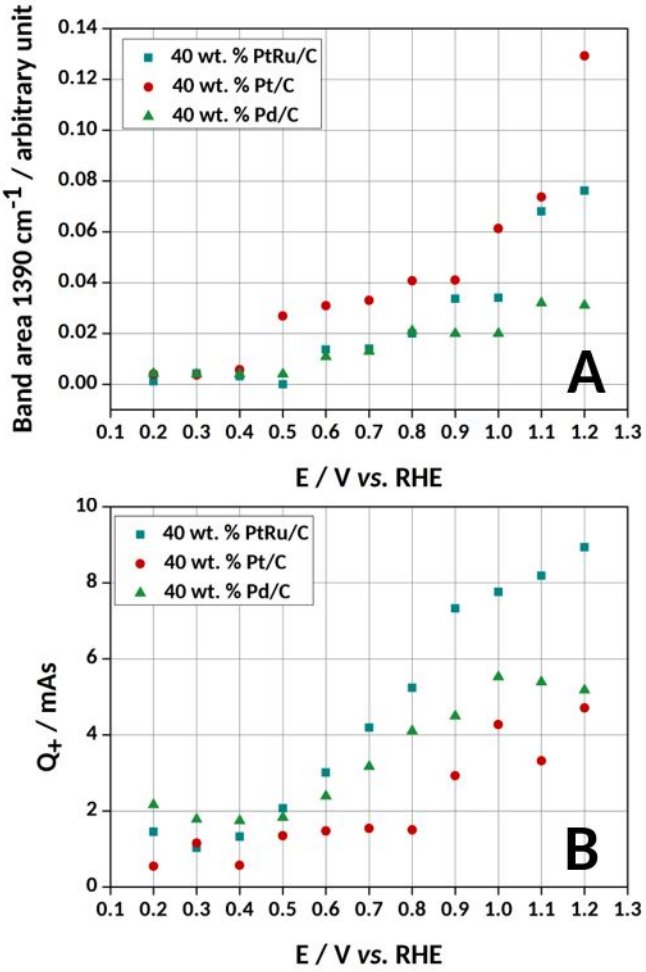

Figure 9. A) Area developed by the 1390 cm^{-1} band at different electrode potential on 40 wt. % PtRu/C, 40 wt. % Pt/C and 40 wt. % Pd/C and B) corresponding electrical charge associated to each oxidation potential step.

4. CONCLUSIONS

In this work, we shed fundamental light on the origin of the detachment of Pt-based NPs occurring during an AST in alkaline media using *in situ* FTIR spectroscopy, *ex situ* XPS and IL-TEM. The presence of carbonate features on the FTIR spectra implies that the degradation mechanism of Pt-based/C nanocatalysts involves the production of carbonates. Thanks to the stepwise oxidation electrochemical protocol, it was shown that carbonates are produced above *E*

= 0.5 V *vs.* RHE for high metal wt. % and above E = 0.8 V *vs.* RHE for low metal wt. %. In addition, no carbonate features were detected on the FTIR spectra for the bare Vulcan XC72 (without Pt NPs), demonstrating that the carbonate formation is promoted by the presence of the Pt NPs at the carbon surface. As a result, one can now strongly affirm that Pt NPs assist the corrosion of the carbon support into CO_2, eventually leading to the local production of solid carbonates at the vicinity of the NPs and the carbon support (at least in electrolytes compatible with metal carbonates formation, *i.e.* NaOH, LiOH, KOH, *etc*.). These carbonates in turn destroy the anchoring sites between the NPs and their support, therefore leading to NP detachment. Combining FTIR spectroscopy and CO_{ads} stripping measurements, a straightforward relationship emerged between the ability of a material to electrooxidize CO_{ads} into CO_2 (to form carbonates at low potential) and the extent of NP detachment. As an example, a more pronounced extent of NPs detachment is reported for PtRu/C (with respect to Pt/C and Pd/C), which is able to oxidize CO at lower potential than Pt/C and Pd/C. We thus conclude that the degradation mechanism is, to some extent, similar for PtRu/C, Pt/C and Pd/C, and the extent of degradation simply depend on the ability of the metal NPs to electrooxidize CO-containing surface groups present on the carbon support.

ASSOCIATED CONTENT

Supporting Information: the SI are composed of four figures

- An example of the baseline correction for the band integration of the FTIR spectra
- The FTIR spectra obtained on polycrystalline Au
- FTIR spectra obtained in the course of an AST consisting of 150 cycles between E = 0.1 and 1.23 V vs. RHE at 100 mV s-1 in 0.1 M NaOH on Vulcan XC72

- C1s and O1s XPS spectra obtained pre and post an AST on 40 wt. % Pt/C and Vulcan XC72

AUTHOR INFORMATION

Corresponding Author

Clémence Lafforgue, clemence.lafforgue@lepmi.grenoble-inp.fr

Frédéric Maillard, frederic.maillard@lepmi.grenoble-inp.fr

Marian Chatenet, marian.chatenet@lepmi.grenoble-inp.fr

ACKNOWLEDGMENT

The authors thank the US Office of Naval Research Global (ONRG) for funding the thesis of Clémence Lafforgue (grant number N62909-16-1-2137). This work was performed within the framework of the Centre of Excellence of Multifunctional Architectured Materials "CEMAM" no. ANR-10-LABX-44-01. M.C. thanks the French IUF for its support.

ABBREVIATIONS

FTIR, Fourier-Transform Infrared Spectroscopy; IL-TEM, Identical Location Transmission Electron Microscopy; PGM, Platinum Group Metal; AFC, Alkaline Fuel Cell; AWE, Alkaline Water Electrolyzer; ORR, Oxygen Reduction Reaction; OER, Oxygen Evolution Reaction; RHE, Reversible Hydrogen Electrode; ECSA, Electrochemical Surface Area; NPs, Nanoparticles; XPS, X-ray Photoelectron Spectroscopy; STEM, Scanning Transmission Electron Microscopy; X-EDS, X-ray Energy Dispersive Spectroscopy; AST, Accelerated Stress Test; IPA, Isopropyl Alcohol; wt. %, weight fraction

REFERENCES

(1) Ghoniem, A. F. Needs, Resources and Climate Change: Clean and Efficient Conversion Technologies. *Prog. Energy Combust. Sci.* **2011**, *37*, 15–51.

(2) Götz, M.; Lefebvre, J.; Mörs, F.; McDaniel Koch, A.; Graf, F.; Bajohr, S.; Reimert, R.; Kolb, T. Renewable Power-to-Gas: A Technological and Economic Review. *Renew. Energy* **2016**, *85*, 1371–1390.

(3) He, Q.; Cairns, E. J. Review—Recent Progress in Electrocatalysts for Oxygen Reduction Suitable for Alkaline Anion Exchange Membrane Fuel Cells. *J. Electrochem. Soc.* **2015**, *162*, F1504–F1539.

(4) Tarasevich, M. R.; Davydova, E. S. Nonplatinum Cathodic Catalysts for Fuel Cells with Alkaline Electrolyte (Review). *Russ. J. Electrochem.* **2016**, *52*, 193–219.

(5) Serov, A.; Zenyuk, I. V.; Arges, C. G.; Chatenet, M. Hot Topics in Alkaline Exchange Membrane Fuel Cells. *J. Power Sources* **2018**, *375*, 149–157.

(6) Gottesfeld, S.; Dekel, D. R.; Page, M.; Bae, C.; Yan, Y.; Zelenay, P.; Kim, Y. S. Anion Exchange Membrane Fuel Cells: Current Status and Remaining Challenges. *J. Power Sources* **2018**, *375*, 170–184.

(7) Marini, S.; Berrettoni, M.; Salvi, P.; Kiros, Y.; Pesenti, R.; Villa, M.; Zangari, G.; Nelli, P. Advanced Alkaline Water Electrolysis. *Electrochim. Acta* **2012**, *82*, 384–391.

(8) Schalenbach, M.; Zeradjanin, A. R.; Kasian, O.; Cherevko, S.; Mayrhofer, K. J. J. A Perspective on Low-Temperature Water Electrolysis - Challenges in Alkaline and Acidic Technology. *Int. J. Electrochem. Sci.* **2018**, *13*, 1173–1226.

(9) Spendelow, J. S.; Wieckowski, A. Electrocatalysis of Oxygen Reduction and Small Alcohol Oxidation in Alkaline Media. *Phys. Chem. Chem. Phys.* **2007**, *9*, 2654–2675.

(10) Serov, A.; Martinez, U.; Atanassov, P. Novel Pd-In Catalysts for Alcohols Electrooxidation in Alkaline Media. *Electrochem. commun.* **2013**, *34*, 185–188.

(11) Sadiki, A.; Vo, P.; Hu, S.; Copenhaver, T. S.; Scudiero, L.; Ha, S.; Haan, J. L. Increased Electrochemical Oxidation Rate of Alcohols in Alkaline Media on Palladium Surfaces Electrochemically Modified by Antimony, Lead, and Tin. *Electrochim. Acta* **2014**, *139*, 302–307.

(12) Ma, J.; Choudhury, N. A.; Sahai, Y. A Comprehensive Review of Direct Borohydride Fuel Cells. *Renew. Sustain. Energy Rev.* **2010**, *14*, 183–199.

(13) Serov, A.; Kwak, C. Direct Hydrazine Fuel Cells: A Review. *Appl. Catal. B Environ.* **2010**, *98*, 1–9.

(14) Serov, A.; Padilla, M.; Roy, A. J.; Atanassov, P.; Sakamoto, T.; Asazawa, K.; Tanaka, H. Anode Catalysts for Direct Hydrazine Fuel Cells: From Laboratory Test to an Electric Vehicle. *Angew. Chemie - Int. Ed.* **2014**, *53*, 10336–10339.

(15) Dekel, D. R. Review of Cell Performance in Anion Exchange Membrane Fuel Cells. *J. Power Sources* **2018**, *375*, 158–169.

(16) Varcoe, J. R.; Atanassov, P.; Dekel, D. R.; Herring, A. M.; Hickner, M. A.; Kohl, P. A.; Kucernak, A. R.; Mustain, W. E.; Nijmeijer, K.; Scott, K.; Xu, T.; Zhuang, L. Anion-Exchange Membranes in Electrochemical Energy Systems. *Energy Environ. Sci.* **2014**, *7*, 3135–3191.

(17) Amar, M.; Dekel, D. R.; Srebnik, S.; Dhara, S.; Pusara, S.; Diesendruck, C. E.; Willdorf, S.; Ash, U. The Critical Relation between Chemical Stability of Cations and Water in Anion Exchange Membrane Fuel Cells Environment. *J. Power Sources* **2017**, *375*, 351–360.

(18) Dekel, D. R.; Rasin, I. G.; Page, M.; Brandon, S. Steady State and Transient Simulation of Anion Exchange Membrane Fuel Cells. *J. Power Sources* **2018**, *375*, 191–204.

(19) Chatenet, M.; Aurousseau, M.; Durand, R.; Andolfatto, F. Silver-Platinum Bimetallic Catalysts for Oxygen Cathodes in Chlor-Alkali Electrolysis - Comparison with Pure Platinum. *J. Electrochem. Soc.* **2003**, *150*, D47–D55.

(20) Olu, P. Y.; Deschamps, F.; Caldarella, G.; Chatenet, M.; Job, N. Investigation of Platinum and Palladium as Potential Anodic Catalysts for Direct Borohydride and Ammonia Borane Fuel Cells. *J. Power Sources* **2015**, *297*, 492–503.

(21) Roche, I.; Chaînet, E.; Chatenet, M.; Vondrák, J. Durability of Carbon-Supported Manganese Oxide Nanoparticles for the Oxygen Reduction Reaction (ORR) in Alkaline Medium. *J. Appl. Electrochem.* **2008**, *38* (9), 1195–1201.

(22) Zadick, A.; Dubau, L.; Sergent, N.; Berthomé, G.; Chatenet, M. Huge Instability of Pt/C Catalysts in Alkaline Medium. *ACS Catal.* **2015**, *5*, 4819–4824.

(23) Zadick, A.; Dubau, L.; Demirci, U. B.; Chatenet, M. Effects of Pd Nanoparticle Size and Solution Reducer Strength on Pd/C Electrocatalyst Stability in Alkaline Electrolyte. *J. Electrochem. Soc.* **2016**, *163*, F781–F787.

(24) Lafforgue, C.; Chatenet, M.; Dubau, L.; Dekel, D. R. Accelerated Stress Test of Pt/C Nanoparticles in an Interface with an Anion-Exchange Membrane - an Identical-Location

Transmission Electron Microscopy Study. *ACS Catal.* **2018**, *8* (2), 1278–1286.

(25) Lafforgue, C.; Zadick, A.; Dubau, L.; Maillard, F.; Chatenet, M. Selected Review of the Degradation of Pt and Pd-Based Carbon-Supported Electrocatalysts for Alkaline Fuel Cells: Towards Mechanisms of Degradation. *Fuel Cells* **2018**, *18*, 229–238.

(26) Pourbaix, M. *Atlas of Electrochemical Equilibria in Aqueous Solutions*; National Association of Corrosion Engineers, Ed.; Houston, 1979.

(27) Ross, P. N.; Sokol, H. The Corrosion of Carbon Black Anodes in Alkaline Electrolyte I. Acetylene Black and the Effect of Cobalt Catalyzation. *J. Electrochem. Soc.* **1984**, *131*, 1742–1750.

(28) Staud, N.; Ross, P. N. The Corrosion of Carbon Black Anodes in Alkaline Electrolyte II. Acetylene Black and the Effect of Oxygen Evolution Catalysts on Corrosion. *J. Electrochem. Soc.* **1986**, *133*, 1079–1084.

(29) Ross, P. N.; Sattler, M. The Corrosion of Carbon Black Anodes in Alkaline Electrolyte III. The Effect of Graphitization on the Corrosion Resistance of Furnace Black. *J. Electrochem. Soc.* **1988**, *135*, 1464–1470.

(30) Staud, N.; Harvey, S.; Ross, P. N. The Corrosion of Carbon Black Anodes in Alkaline Electrolyte IV. Current Efficiencies for Oxygen Evoltion from Metal Oxide-Impregnated Graphitized Furnace Blacks. *J. Electrochem. Soc.* **1989**, *136*, 3570–3576.

(31) Herrmann, C. C.; Perrault, G. G.; Pilla, A. A. Dual Reference Electrode for Electrochemical Pulse Studies. *Anal. Chem.* **1968**, *40*, 1173–1174.

(32) Garsany, Y.; Singer, I. L.; Swider-Lyons, K. E. Impact of Film Drying Procedures on RDE

Characterization of Pt/VC Electrocatalysts. *J. Electroanal. Chem.* **2011**, *662*, 396–406.

(33) Iwasita, T.; Nart, F. In Situ Infrared Spectroscopy at Electrochemical Interfaces. *Prog. Surf. Sci.* **1997**, *55*, 271–340.

(34) Iwasita, T.; Rodes, A.; Pastor, E. Vibrational Spectroscopy of Carbonate Adsorbed on Pt(111) and Pt(110) Single-Crystal Electrodes. *J. Electroanal. Chem.* **1995**, *383*, 181–189.

(35) Oliver, B. G.; Davis, A. R. Vibrational Spectroscopic Studies of Aqueous Alkali Metal Bicarbonate and Carbonate Solutions. *Can. J. Chem.* **2006**, *51*, 698–702.

(36) Su, C.; Suarez, D. L. In Situ Infrared Speciation of Adsorbed Carbonate on Aluminium and Iron Oxides. *Clays Clay Miner.* **1997**, *45*, 814–825.

(37) García, G.; Rodríguez, P.; Rosca, V.; Koper, M. T. M. Fourier Transform Infrared Spectroscopy Study of CO Electro-Oxidation on Pt(111) in Alkaline Media. *Langmuir* **2009**, *25*, 13661–13666.

(38) Chang, S. C.; Ho, Y.; Weaver, M. J. Applications of Real-Time FTIR Spectroscopy to the Elucidation of Complex Electroorganic Pathways: Electrooxidation of Ethylene Glycol on Gold, Platinum, and Nickel in Alkaline Solution. *J. Am. Chem. Soc.* **1991**, *113*, 9506–9513.

(39) Godoi, D. R. M.; Villullas, H. M.; Zhu, F. C.; Jiang, Y. X.; Sun, S. G.; Guo, J.; Sun, L.; Chen, R. A Comparative Investigation of Metal-Support Interactions on the Catalytic Activity of Pt Nanoparticles for Ethanol Oxidation in Alkaline Medium. *J. Power Sources* **2016**, *311*, 81–90.

(40) Socrates, G. *Infrared and Raman Characteristic Group Frequencies*; John Wiley & Sons

Ltd, 2001.

(41) Kinoshita, K. *Carbon Electrochemical and Physicochemical Properties*; John Wiley & sons, I., Ed.; 1988.

(42) Fanning, P. E.; Vannice, M. A. A DRIFTS Study of the Formation of Surface Groups on Carbon by Oxidation. *Carbon N. Y.* **1993**, *31*, 721–730.

(43) Zawadzki, J. Infrared Studies Of Aromatic Compounds Adsorbed Oh The Surface Of Carbon Films. *Carbon N. Y.* **1988**, *26*, 603–611.

(44) Zawadzki, J. IR Spectroscopy Studies of Oxygen Surface Compounds on Carbon. *Carbon N. Y.* **1978**, *16*, 491–497.

(45) Meldrum, B. J.; Rochester, C. H. In Situ Infrared Study of the Surface Oxidation of Activated Carbon Dispersed in Potassium Bromide. *J. Chem. Soc. Faraday Trans.* **1990**, *86*, 2997–3002.

(46) Ishizaki, C.; Marty, I. Surface Oxide Structures On A Commercial Activated Carbon. *Carbon N. Y.* **1981**, *19*, 409–412.

(47) Castanheira, L.; Dubau, L.; Mermoux, M.; Berthomé, G.; Caqué, N.; Rossinot, E.; Chatenet, M.; Maillard, F. Carbon Corrosion in Proton-Exchange Membrane Fuel Cells: From Model Experiments to Real-Life Operation in Membrane Electrode Assemblies. *ACS Catal.* **2014**, *4*, 2258–2267.

(48) Castanheira, L.; Silva, W. O.; Lima, F. H. B.; Crisci, A.; Dubau, L.; Maillard, F. Carbon Corrosion in Proton-Exchange Membrane Fuel Cells: Effect of the Carbon Structure, the Degradation Protocol, and the Gas Atmosphere. *ACS Catal.* **2015**, *5*, 2184–2194.

(49) Maillard, F.; Bonnefont, A.; Micoud, F. An EC-FTIR Study on the Catalytic Role of Pt in Carbon Corrosion. *Electrochem. commun.* **2011**, *13*, 1109–1111.

(50) Maillard, F.; Savinova, E. R.; Simonov, P. A.; Zaikovskii, V. I.; Stimming, U. Infrared Spectroscopic Study of CO Adsorption and Electro-Oxidation on Carbon-Supported Pt Nanoparticles: Interparticle versus Intraparticle Heterogeneity. *J. Phys. Chem. B* **2004**, *108*, 17893–17904.

(51) Štrbac, S.; Adžić, R. R. The Influence of OH- Chemisorption on the Catalytic Properties of Gold Single Crystal Surfaces for Oxygen Reduction in Alkaline Solutions. *J. Electroanal. Chem.* **1996**, *403*, 169–181.

(52) Yi, Y.; Weinberg, G.; Prenzel, M.; Greiner, M.; Heumann, S.; Becker, S.; Schlögl, R. Electrochemical Corrosion of a Glassy Carbon Electrode. *Catal. Today* **2017**, *295*, 32–40.

(53) Chattot, R.; Asset, T.; Bordet, P.; Drnec, J.; Dubau, L.; Maillard, F. Beyond Strain and Ligand Effects: Microstrain-Induced Enhancement of the Oxygen Reduction Reaction Kinetics on Various PtNi/C Nanostructures. *ACS Catal.* **2017**, *7*, 398–408.